Phys. Status Solidi B **249**, No. 4, 752–763 (2012) / **DOI** 10.1002/pssb.201100771

physica status solidi b
www.pss-b.com
basic solid state physics

Feature Article

Site-controlled SiGe islands on patterned Si(001): Morphology, composition profiles, and devices

Jianjun Zhang*[,1], Armando Rastelli[1], Oliver G. Schmidt[1], and Günther Bauer[2]

[1] Institute for Integrative Nanosciences, IFW Dresden, Helmholtzstr. 20, 01069 Dresden, Germany
[2] Institute of Semiconductor and Solid State Physics, University Linz, 4040 Linz, Austria

Received 1 November 2011, revised 9 January 2012, accepted 13 January 2012
Published online 21 February 2012

Keywords composition, morphology, ordered islands, silicon-germanium

* Corresponding author: e-mail j.zhang@ifw-dresden.de, Phone: +49 351 4659864, Fax: +49 351 4659782

Deterministic control of position on a substrate, uniform size and shape are prerequisite for most of the envisioned applications of SiGe islands in electronic and optoelectronic devices. As an example of electronic application, tensile strained Si layers on top of coherent SiGe islands may be used as channels for field effect transistors (FETs) with enhanced electron mobility. For such a kind of application, site-controlled islands are required to allow for their external addressability. In this feature article we investigate the morphological and compositional evolution of site-controlled SiGe islands on pit-patterned Si(001) substrates. We then report on the first demonstrated n-channel FET with enhanced electron mobility based on SiGe islands. Finally, a new approach for further increase of the tensile strain is presented.

1 Introduction Strain driven self-assembly of defect-free three-dimensional (3D) Ge or SiGe islands on Si(001) substrates is an active topic of both fundamental and practical interest [1]. Fundamentally, the Ge/Si(100) material system is regarded as prototypical for investigating the basic phenomena leading to the formation of "self-assembled quantum dots" [2–10]. Technologically, the Ge/Si(100) system is of interest for possible applications in electronic [11–14], thermoelectric [15], and optoelectronic devices [16, 17]. For the latter it is particularly interesting for detection of light in the 1.5 μm wavelength range and its convenient integration with the mature Si technology [16].

SiGe islands can be obtained by epitaxial growth of Ge on a Si(001) substrate. After completion of a pseudomorphic wetting layer, 3D islands form to partially release the elastic energy due to the lattice mismatch. At relatively high substrate temperatures, growing islands evolve from unfaceted prepyramids to truncated pyramids (TPs), pyramids (Ps), domes (Ds), and eventually barns (Bs) before plastic relaxation occurs [8]. When the epitaxial growth is performed on planar substrates, the island ensembles are characterized by rather broad size and shape distributions due to the statistical nature of the self-assembling process [3–6]. Island coarsening, consisting in the growth of larger islands at the expense of smaller ones through material exchange, also contributes to the broadening of the distributions [7, 9]. However, for most of the envisioned applications, site-controlled islands with uniform size and shape are compulsory. For instance, tensile strained Si layers on top of coherent SiGe islands may be used as channels for n-channel metal–oxide–semiconductor field effect transistors (MOSFETs) with enhanced electron mobility [11].

In order to obtain perfectly ordered island arrays, new approaches have been developed, which are based on the combination of lithography and self-assembling techniques [18]. Long range ordering in one [19–21] or two dimensions using either selective epitaxial growth through oxide masks [22] or direct growth on pit-patterned substrates [23–25] was successfully demonstrated and excellent size homogeneities were reported [26]. Here, we focus on the latter approach. Several parameters and processing steps can be used to tailor the properties of the resulting islands, such as pit morphology and density, amount of deposited Ge and substrate temperature. In addition, *in situ* postgrowth annealing promotes relevant changes in the island morphology and composition. On planar Si(001) substrates

it has been found that islands with steep facets transform back to shallower pyramids [27–29] as they intermix with Si from the substrate. This intermixing occurs via lateral island motion, which is driven by surface mediated alloying [9, 28, 29]. Additionally, island coarsening takes place, which leads to a drop in island density and a broadening of the island size distribution due to material exchange via surface diffusion. It is therefore interesting to study the influence of the pits on the island evolution during annealing and to test whether annealing can be used to further engineer the properties of site-controlled islands.

The alloy distribution in strained epitaxial islands is crucial in determining their optical and electronic properties. The composition has been experimentally probed by various methods, such as anomalous X-ray scattering [30–32], X-ray photoelectron microscopy [33, 34], cross-sectional transmission electron microscopy (TEM) combined with electron energy loss spectroscopy [35, 36], cross-sectional scanning tunneling microscopy [37], and by analyzing the deformation induced by buried islands on the surface of the capping layer [38]. Some of these techniques can access the composition by averaging over a statistical ensemble of islands, thus neglecting possible island-to-island variations [30, 32, 39]. Others are limited to cross-sectional profiles [35–37] or only to the surface composition [33, 34]. Electron tomography using Z-contrast imaging in scanning TEM [40, 41] is a promising approach to obtain composition maps of single islands, but the method has not provided absolute composition values so far. Very recently, the composition of single SiGe islands [42] and quantum-dot molecules [43] has been successfully characterized by using a focused synchrotron X-ray beam with sub-microsizes. Nanotomography, which combines selective wet chemical etching and atomic force microscopy (AFM), is a relatively simple tool to obtain quantitative 3D alloy distribution of individual SiGe islands [44]. The reliability of the compositional values obtained by nanotomography was confirmed by anomalous X-ray scattering measurements in grazing-incidence performed at the ID01 beamline of the European Synchrotron Radiation Facility [44] and by coplanar X-ray diffraction (XRD) measurements [45]. Here, we investigate the composition profiles of site-controlled islands by using nanotomography.

The strain alters the band structure of Si [46–48] and, since the 90 nm technology node, the strain-enhanced mobility has been utilized to increase the output current in MOSFET devices [49]. In n-channel MOSFETs, enhanced electron mobility was successively demonstrated by using a buried $Si_{1-x}Ge_x$ layer to induce tensile strain on the overlying Si channel [12, 13]. The strain in the Si channel depends on the Ge fraction, thickness and width of the SiGe layer [12, 50]. However, in SiGe layers, the maximum Ge content for a given thickness is limited by the onset of plastic relaxation [46]. The advantage of SiGe islands over planar SiGe layers is that islands only induce strain locally in the Si channel and they can therefore have a larger Ge content while preserving crystal perfection. This motivates the realization of n-channel MOSFETs on buried SiGe islands, referred to as DotFET [11].

The paper is organized as follows: we investigate the morphological (Section 2) and compositional (Section 3) evolution of as-grown and annealed SiGe islands on patterned Si(001) substrates with the same and with different pit periods along the two orthogonal $\langle 110 \rangle$ directions; in Section 4 we report on the first demonstration of n-channel DotFET with enhanced electron mobility; in Section 5 a new approach is presented allowing to further enhance the tensile strain in the Si channel, and consequently to enhance the electron mobility.

2 Morphology

2.1 Morphological evolution of SiGe islands on pit-patterned substrates 2D arrays of pits were patterned onto 4 inches Si(001) wafers by optical lithography and reactive ion etching (RIE). Each wafer consists of 54 dies and each die contains four patterned fields of size 1.5 mm × 1.5 mm with periods of 600, 800, 900, and 1000 nm. After cutting the wafer into 9.0 mm × 9.0 mm dies and *ex situ* chemical cleaning, the samples were dipped in a diluted hydrofluoric acid (HF) solution to create a hydrogen terminated surface. After *in situ* out-gassing at 620 °C, the substrate temperature was decreased to 360 °C and a Si buffer layer was deposited at a rate of 0.6 Å/s using solid source molecular beam epitaxy (MBE). The Ge was deposited at 700 °C at a rate of 0.05 Å/s. The surface morphology was investigated using AFM operating in tapping mode at room temperature (RT).

The pits after patterning are circular and have an average depth and diameter of about 84 and 300 nm, respectively. After deposition of a 36 nm thick Si buffer, the circular pits evolve into a multifaceted shape with {103}, {113}, and {11n} facets. Meanwhile, their depth decreases while their diameter increases [51]. After 3 monolayers (ML) Ge deposition, the multifaceted pits transform into inverted pyramids with {105} facets [52].

Figure 1 shows AFM images obtained after deposition of various amounts of Ge at 700 °C on top of a 36 nm thick Si buffer layer. For all Ge coverages considered here (3.75–6 ML) arrays of islands with *homogeneous* shape are observed only at the pit bottoms, while no islands form between the patterned pits. We thus obtain a perfect lateral ordering in two dimensions independently on the amount of deposited Ge. (We note that the slight misalignment of every second row of the ordered islands is due to the optical mask shift during the process of the double patterning of the substrate.)

If the growth is stopped at 3.75 ML Ge [Fig. 1(a)], a 2D array of TPs is obtained. This is a remarkable result, since on planar Si(001) surfaces TPs are usually observed together with other island shapes (Ps or Ds) [8, 53]. When the Ge coverage increases further, steeper morphologies appear [Fig. 1(b) and (c)]. It is noteworthy that perfectly ordered arrays of SiGe islands can be obtained with pattern periods between 600 and 1000 nm [Fig. 1(c) and (d)].

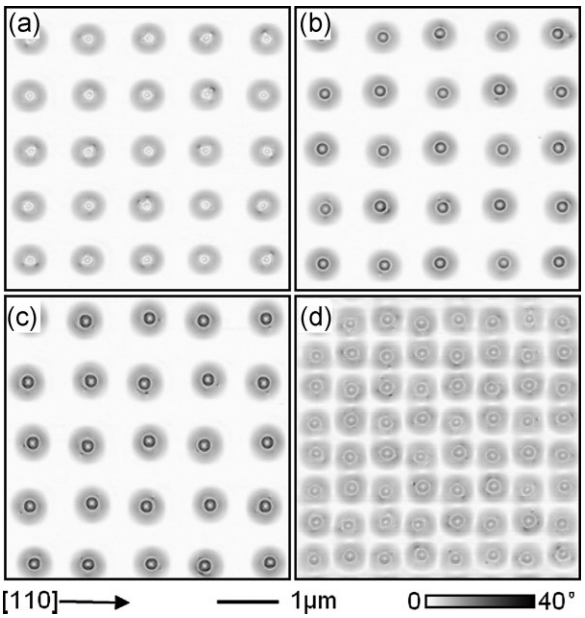

Figure 1 AFM images obtained upon deposition of 36 nm Si and subsequent deposition of 3.75 ML Ge (a), 5.0 ML Ge (b), and 6 ML Ge on a pit-patterned substrate with period of 1000 nm (c) and of 6 ML Ge on pits with period of 600 nm (d). The Ge growth was performed at a substrate temperature of 700 °C [51].

Figure 2 shows AFM images of individual SiGe islands obtained after deposition of 3.75 ML (a), 4 ML (b), 5 ML (c), 6 ML (d), 7 ML (e), and 8.0 ML (f) Ge at 700 °C. The islands evolve from pre-pyramids (not shown here) to TPs [Fig. 2(a)] containing a top surface with orientation close to the (001) and {105} side facets and eventually to mature pyramids bounded by four {105} facets [Fig. 2(b)]. The pit sidewalls

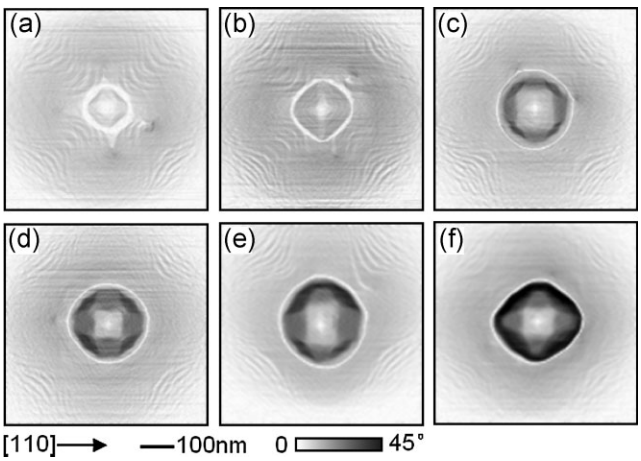

Figure 2 AFM images of individual SiGe islands obtained upon deposition of a 36 nm thick Si buffer and subsequent deposition of 3.75 ML Ge (a), 4 ML Ge (b), 5 ML Ge (c), 6 ML Ge (d), 7 ML Ge (e), and 8.0 ML Ge at 700 °C on a pit-patterned substrate with period of 1000 nm (f). The shading allows shallow and steep facets to be distinguished according to the local surface slope with respect of the (001) plane [51].

are decorated by {105} facets and steps, similar to the morphologies reported previously [54]. Interestingly, the transitional dome [Fig. 2(c)] appears *symmetric* while on planar Si(001) surfaces, the transitional domes follow a series of asymmetric shapes [5, 6]. When the Ge coverage increases further, the transitional domes evolve into domes bounded by {105}, {113}, and {15 3 23} facets [Fig. 2(d)]. Finally, the latter change their shape and evolve into another transitional structure [Fig. 2(e)] before reaching the barn shape after deposition of 8.0 ML Ge [Fig. 2(f)]. In addition to the dome related facets, steeper {111} as well as {20 4 23} facets are observed at their base. This evolution is similar to that reported recently for SiGe islands on planar Si(001) substrates [8, 55].

Therefore, the presence of an ordered pattern produces islands with similar sizes, and consequently with similar shapes. (In an equilibrium picture the island shape is a function of island volume and composition [8].) On planar substrates, coarsening of larger/steeper islands at the expense of smaller/shallower islands [7, 8] renders it difficult to produce ensembles of islands with the same shape. The observation of homogeneous arrays of TPs on the patterned substrate indicates that coarsening is strongly suppressed with respect to growth on planar substrates. Coarsening takes place when islands with different sizes are able to exchange material [7, 9]. Pit-patterned substrates favor on one hand equal distribution of the deposited material, which results in improved size homogeneity, thus limiting the driving force for coarsening. On the other hand the presence of pits may hinder material exchange between islands. Although (within our growth conditions) the adatom migration length is larger than the distance between pits and the probability of adatom detachment from an island is probably not affected by the presence of a pit, the pit does affect the surface diffusion of adatoms away from an island. Since each pit represents a local minimum of the chemical potential due to local surface curvature, we imagine that adatoms detaching from an island get incorporated again into the same island before possibly moving to other islands and produce coarsening of the ensemble. The large pit depth (about 60 nm) used in our experiment is also responsible for such a behavior. In fact, in our further investigations we found that shallower pits are not able to prevent coarsening.

Within the capture zone picture we can also rationalize the observation of symmetric TDs. Asymmetric shapes observed on planar surfaces are attributed to asymmetries in the neighborhood of the islands [5]. Since the shape of pits after buffer growth has fourfold symmetry and the pits are periodically distributed, we expect the flux of Ge contributing to island growth to be isotropic and to favor the development of fourfold symmetric structures.

2.2 Morphologies of SiGe islands on patterned substrates with different pit periods along the two orthogonal ⟨110⟩ directions Most of the studies reported so far have been performed on islands arranged in 2D square (or close to square) lattices. In order to guarantee

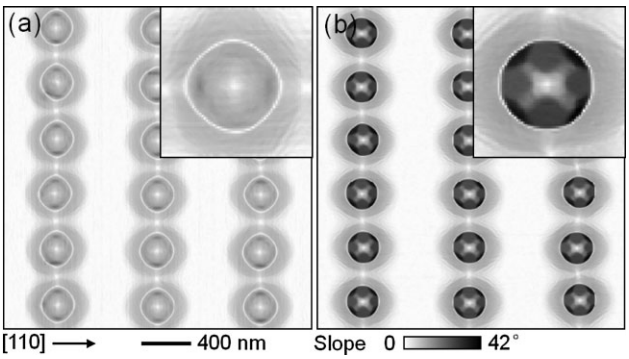

Figure 3 AFM images of SiGe islands obtained upon deposition of 6 ML (a) and 8 ML (b) Ge at 720 °C on patterned pits with periods of 400 and 800 nm along the two orthogonal ⟨110⟩ directions. Insets are individual islands with higher magnification.

design flexibility and investigate the limits of site-control, it is important to study the effect of reduced pattern symmetry on the island properties. To this aim we consider here a rectangular lattice of pits with different periods along the two orthogonal ⟨110⟩ directions. Ge is deposited on electron-beam patterned substrates with pits arranged in a rectangular mesh with a 400 nm × 800 nm "unit cell". The pits have a depth of about 75 nm and a diameter of about 180 nm. The deposited Si buffer is 36 nm and the deposition rates for Si and Ge are 1.0 and 0.05 Å/s, respectively. Figures 3(a) and (b) show the AFM images of SiGe islands obtained after the deposition of 6 and 8 ML Ge at 720 °C, respectively. The pit sidewalls are decorated by {105}-facets and steps, similar to the morphologies shown in Fig. 2. Insets are individual islands with higher magnification, showing that the islands are symmetric. Although the periodic pits are only twofold symmetric and we may expect the Ge fluxes from the two orthogonal ⟨110⟩ directions to be different, no asymmetric islands are observed. We will discuss a possible explanation in Section 3.2.

2.3 Morphological transition of SiGe islands after annealing As mentioned in the introduction, post-growth annealing may be used to further engineer the properties of site-controlled islands. For this experiment, 2D pit arrays with a period of 400 nm were patterned by holographic lithography and RIE. The samples were cleaned and dipped in a diluted HF solution (as described in Section 2.1) before loading to MBE system. After a 36 nm Si buffer growth, 20 ML Ge were deposited at 720 °C at a rate of 0.03 Å/s and then the sample was kept at 720 °C for 20 min before cooling to RT.

Figure 4 shows AFM images of samples obtained after deposition of 20 ML Ge at 720 °C [Fig. 4(a)] and after subsequent *in situ* annealing for 20 min [Fig. 4(b)] [56]. After the deposition of 20 ML Ge at 720 °C, a perfect site-controlled array of barn-shaped islands is observed. After 20 min *in situ* annealing, the barns have transformed into pyramids, as demonstrated by the surface orientation maps

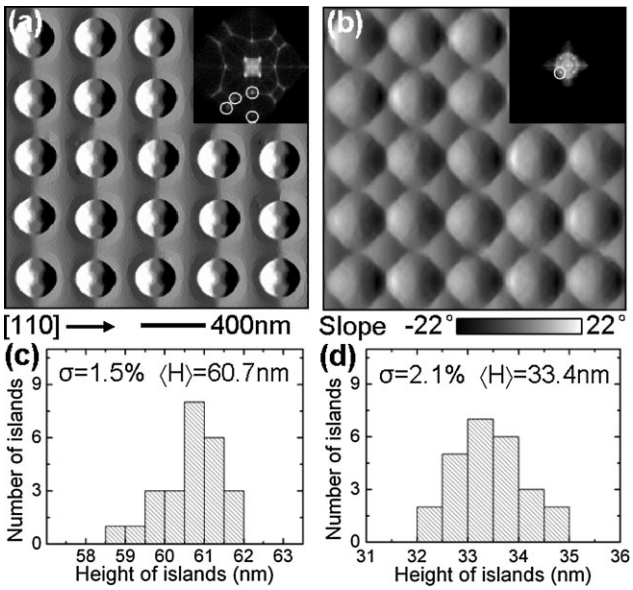

Figure 4 AFM images of islands obtained by deposition of 20 ML Ge at 720 °C on a pit-patterned Si(001) substrate with a period of 400 nm (a) and of islands grown with same nominal parameters followed by *in situ* annealing at 720 °C for 20 min (b). The grayscale represents the first derivative along the horizontal axis. The insets show surface orientation maps with circles marking the steep barn facets in (a) and shallow {105} facets in (b). The corresponding histograms of island height distribution are shown in (c) and (d), respectively. Average height values ⟨*H*⟩ and relative standard deviation σ of the distributions are quoted. After Ref. [56].

[45, 57] in the insets of Fig. 4(a) and (b). In such plots, the spots associated with the steep facets typical for barns [see circles in the inset of Fig. 4(a)] disappear in favor of large {105} facets [circle in the inset of Fig. 4(b)]. The histograms in Fig. 4(c) and (d) display the island height distribution before and after *in situ* annealing. Annealing reduces substantially the average height ⟨*H*⟩ of the islands. However, the relative width of the size distribution, quantified by the standard deviation σ, does not change much (values are quoted in the figures). The shape change and height reduction reflect the redistribution of material during intermixing, as previously reported for islands on planar substrates [27–29]. However, on planar substrates, annealing also leads to coarsening, *i.e.*, shrinkage of smaller islands in favor of larger islands. As discussed above, the presence of periodically distributed pits creates islands with very similar sizes in a symmetric environment [26, 51, 58]. Therefore, the driving force for coarsening is extremely small, so coarsening is effectively suppressed and the size homogeneity is well preserved.

3 Composition

3.1 Compositional evolution of SiGe islands on patterned substrates The samples discussed in this section were grown by MBE on 2D patterned substrates with a period of 500 nm and pit depths and diameters of about

65 and 350 nm, respectively. After 45 nm of Si buffer layer growth, 3.5, 6.0, 9.0, and 12.0 ML Ge were deposited at a substrate temperature of 720 °C and at a Ge growth rate of 0.03 Å/s [59]. Correspondingly, we obtained uniform arrays of SiGe-filled pits, pyramids, domes, and barns, similar to the morphologies shown in Fig. 2. We note that the amount of Ge required here for obtaining a given island shape is larger than the amount needed for the patterns shown in Fig. 2. The reason is the smaller pit period, and consequent smaller capture zone [51]. The chemical composition profiles of the SiGe islands were determined by a nanotomography technique, which is based on AFM and selective wet chemical etching [44, 57]. The samples were etched at RT in NHH solution [1:1 vol. (28% NH_4OH):(31% H_2O_2)], which selectively etches $Si_{1-x}Ge_x$ alloys over pure Si and shows an etching rate increasing approximately exponentially with the Ge fraction x, no preferential etching direction, and a negligible dependence on strain [60, 61].

Figure 5(a–d) shows a sequence of 3D AFM images of the same surface area obtained after deposition of 12 ML Ge (as-grown barn-shaped islands) and after subsequent selective etching in NHH solution for 100, 280, and 500 min. We see that (i) for all the islands SiGe is etched symmetrically and (ii) the homogeneity of the shape and size of the residual island material is preserved after different etching times. (i) indicates a symmetric Ge distribution for all islands and (ii) demonstrates that different islands in the array have similar composition distributions. To obtain 3D composition profiles, we performed 12 etching steps. Each step results in the removal of about 4–10 nm thick SiGe shell. The uncertainty originates mainly from registering the AFM images after different etching steps and the *relative* uncertainty of the resulting composition profiles is less than 10% [44]. Figure 5(e) and (f), respectively, show the horizontal cross-cuts parallel to the (001) plane of the Ge distribution for islands shown in Fig. 5(a) at heights of 36 and 10 nm, with respect to the level of the island bases. Figure 5(g) shows a vertical cross-section of the Ge composition on the (110) plane passing through the centers of one row of islands. The symmetric Ge distribution is clearly seen and all islands show similar Ge composition profiles within the uncertainties. In contrast, on planar substrates, slight lateral asymmetries in the composition associated with shape asymmetries are observed [44], and the island composition is asymmetric even for islands with an apparently symmetric shape [59]. It is noteworthy that islands grown on planar surfaces differ from islands grown on pit-patterned substrates not only for their asymmetric composition profiles, but also for the values of volume and average Ge content x [59, 62].

Since our etching results show that the island arrays remain homogeneous in shape, size, and composition at all investigated stages of growth, we limit in the following the discussion to the compositional evolution of single islands. Figure 6(a–i) show a sequence of 3D AFM images of individual islands prior to etching and after different etching times in NHH for a pyramid (a–c), a dome (d–f), and a barn (g–i), respectively. For all types of islands, the etching profiles are symmetric after different etching steps, indicating a symmetric Ge distribution. For the pyramid, the material at the edges is etched faster than at the corners [Fig. 6(b)], demonstrating that the corners are enriched with

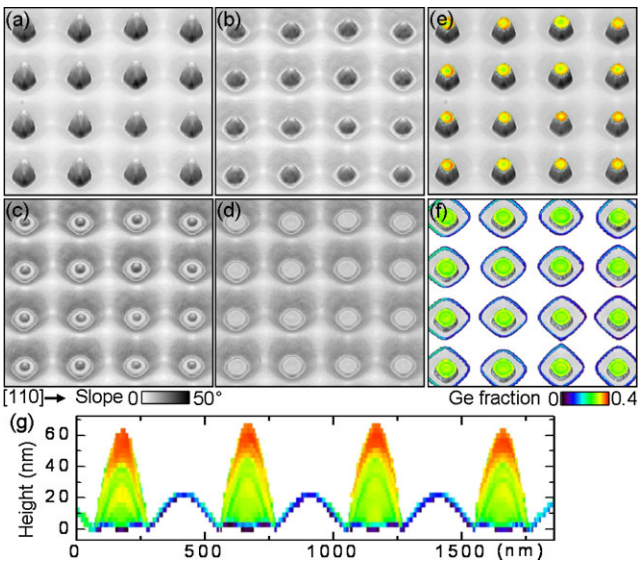

Figure 5 (online color at: www.pss-b.com) Sequence of 3D AFM images of the same surface area obtained after deposition of 12 ML Ge on patterned Si(001) with a period of 500 nm at 720 °C (a) and after selective etching in NHH solution for 100 min (b), 280 min (c), and 500 min (d). (e) and (f) Horizontal cross-cuts of the islands shown in (a) with in-plane Ge compositions at heights of 36 and 10 nm with respect to the level of the island bases. (g) Vertical cross-cut of the Ge content across one island row shown in (a) passing through the island centers along the (110) direction. After Ref. [59].

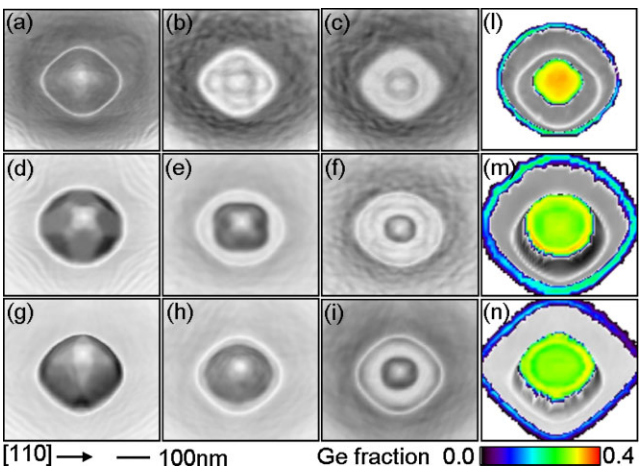

Figure 6 (online color at: www.pss-b.com) Sequences of 3D AFM images of individual islands prior to etching and after different etching times in NHH solution for pyramid (a–c), dome (d–f), and barn (g–i), respectively. (l–n) Horizontal cross-cuts of the pyramid, dome, and barn with in-plane compositions at a height of 10 nm with respect to the level of island bases. After Ref. [59].

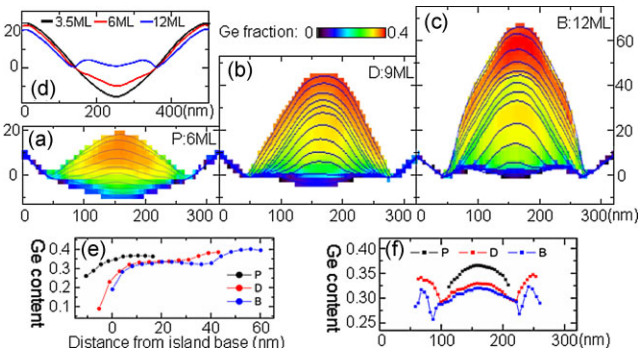

Figure 7 (online color at: www.pss-b.com) Cross-sectional Ge compositions on (110) planes passing through island centers for a pyramid (a), a dome (b), and a barn (c), grown on pit-patterned Si(001) at 720 °C. The level of the island bases is set as zero. (d) Comparison of pit morphologies (AFM linescans passing through pit centers along (110) direction) before nucleation (3.5 ML Ge, black line) and after almost complete SiGe removal in NHH for a pyramid (6 ML Ge, red line) and a barn (12 ML Ge, blue line). (e) and (f) Ge compositions along the growth direction and the lateral (110) direction at a height of 10 nm with respect to the level of island bases, passing through the island centers for pyramid, dome, and barn, respectively.

Si, as previously observed for pyramids on planar substrates [63, 64]. However, these features are not observed for the domes and barns, indicating a Ge redistribution during the evolution from pyramid to dome and barn. Figure 6(l–n) show the in-plane Ge distributions for the different island shapes at a height of 10 nm with respect to the level of the island bases. (For the vertical alignment, we assumed the bases of these islands are at the same level. Our calculations of the amount of Si incorporated into the islands from the surroundings during the island evolution from pyramids to barns have proven that this assumption is reasonable.) Figure 7(a–c) shows AFM linescans obtained at different stages of NHH etching and the derived cross-sectional Ge compositions on (110) planes passing through island centers. Both from the horizontal [Fig. 6(l–n)] and vertical [Fig. 7(a–c)] cross-cuts, we observe that at the bottom of the islands, *e.g.*, at a height of 10 nm above the island base, the Ge fraction drops from about 35 to 31% [see also Fig. 7(e,f)] when a pyramid evolves into a dome, while no clear changes are observed when a dome transforms into a barn. Furthermore, after the almost complete removal of the SiGe in the islands in NHH solution, the bottom of the pit is about 9 nm lower than the island base for the pyramid, while it is only about 5 nm lower than the island base for the dome and is almost at the same level of the island base for the barn, as seen by comparing the bottommost linescans in Fig. 7(a–c). This is further demonstrated in Fig. 7(d) where the bottom linescans of the etched pyramid and barn are shown together with a linescan of a pit after 3.5 ML Ge deposition (*i.e.*, before island formation). These results indicate that the Ge content at the base of the islands decreases as the island grows in size and is less than 10% for the barn-shaped islands after 12 ML Ge.

By assuming that shape transitions from pyramid to dome and from dome to barn are simply accomplished by progressive material accumulation at the island surface in a layer-by-layer fashion [6, 9, 28], we would expect to find a pyramid (or, more precisely, the Ge distribution observed in the pyramid) "inside" the dome and a dome "inside" the barn [44]. However, the comparison of Fig. 7(a–c) and of the linescans of Ge composition along the growth direction shown in Fig. 7(e) indicates that the data are not fully compatible with this picture. In fact, as noted above, the bottom region of the islands becomes Si-richer as pyramids transform into domes and barns. Furthermore, the top and Ge-rich region ($x \sim 38\%$) of the dome is replaced by a Ge-poorer region ($x \sim 32\%$) in the barn, while the underlying Ge rich core is almost preserved. Finally, the horizontal linescans for domes and barns shown in Fig. 7(f) indicate that there is a Si-rich shell (dip in the linescans) which appears to shift outwards when the domes transform to barns.

For islands grown on planar substrates, it has been previously shown that Si–Ge intermixing mainly occurs through surface diffusion and that islands change shape by accumulation of material at their surface [9, 28]. However, the results presented in Fig. 7 (for instance the Si enrichment of the island base) can be hardly explained by surface diffusion only. Although most of the Si incorporated into the islands must come from the surrounding substrate regions, the complex compositional evolution accompanying the island growth suggests that also "intra-island diffusion" occurs during Ge deposition [65]. This phenomenon was reported to take place, even at lower substrate temperatures, during annealing experiments in conditions inhibiting Si surface diffusion [65]. In our case we argue that the pits, by effectively pinning the island positions [56], limit the efficient surface-mediated intermixing which is associated with island motion [28] and asymmetric composition profiles [44, 59]. On the other hand, further experimental and theoretical work is needed to understand the mechanisms responsible for the fine but complex compositional gradients observed in SiGe islands grown on pit-patterned substrates.

3.2 Compositional profiles of SiGe islands on patterned substrates with different pit periods along the two orthogonal ⟨110⟩ directions As discussed in Section 2.2, even in the case of rectangular patterns with different pit periods along the two ⟨110⟩ directions, islands are still symmetric. Since the capture zone of each island is rectangular, we may expect some reduced symmetry also in the composition profiles. We therefore investigated the compositional profile of these islands shown in Fig. 3(b) by nanotomography. Figure 8(a–d) show the sequence of AFM images of the same surface area prior to etching (dome-shaped islands) and after subsequent selective etching in NHH solution for 80, 250, and 500 min. We see that for all the islands the SiGe has been removed symmetrically and the homogeneity of the shape and size of the residual island material is preserved after different etching times, indicating a symmetric Ge distribution for all

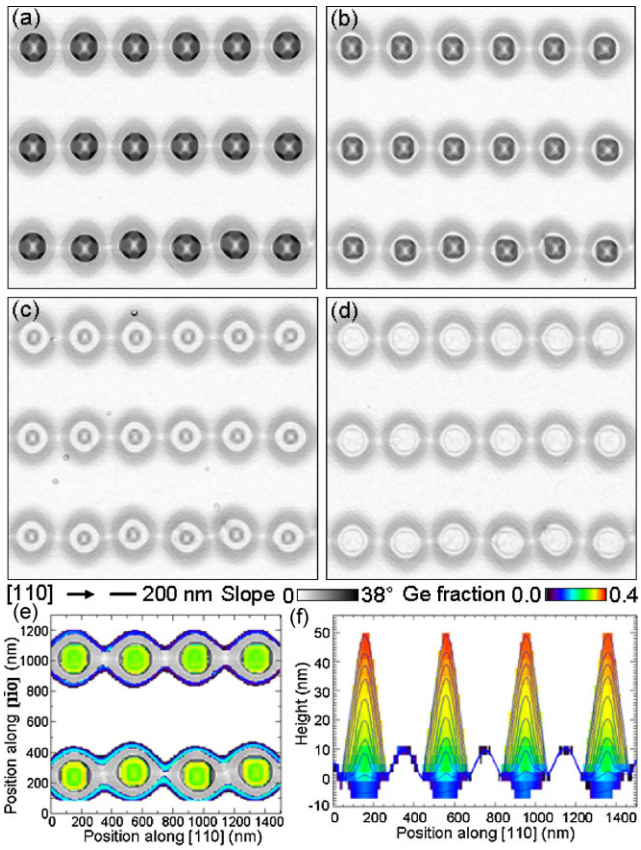

Figure 8 (online color at: www.pss-b.com) Sequence of AFM images of the same surface area obtained after deposition of 8 ML Ge on patterned Si(001) with pit periods of 400 and 800 nm along the two ⟨110⟩ directions at 720 °C (a) and after selectively etched in NHH solution for 80 min (b), 250 min (c), and 500 min (d). (e) Ge composition in the horizontal cross-cut plane at a height of 10 nm with respect to the island bases. (f) Ge composition in vertical cross-cut plane passing through the centers of four islands along (110) direction.

islands and a compositional homogeneity for the arrays. Figure 8(e) shows the Ge composition in the horizontal cross-cut plane at a height of 10 nm with respect to the island bases. Figure 8(f) displays the Ge composition in a vertical cross-cut plane passing through the centers of four islands along (110) direction. Although, it is legitimate to expect an anisotropic Ge flow, we observe symmetric Ge composition profiles, similar to the results on periodic pits with fourfold symmetry (see Fig. 5).

These observations indicate that a symmetric shape and compositional profile are energetically favorable and that, at least at the relatively high growth temperature used here, it is kinetically possible for the Ge (and Si) adatoms to reach any position of the islands during deposition. On the other hand the homogeneity of the island array is not surprising since islands are still at the center of (rectangular) capture zones with nominally the same size. A breakdown of such homogeneity is expected for more complex pit arrangements resulting in dissimilar capture zones.

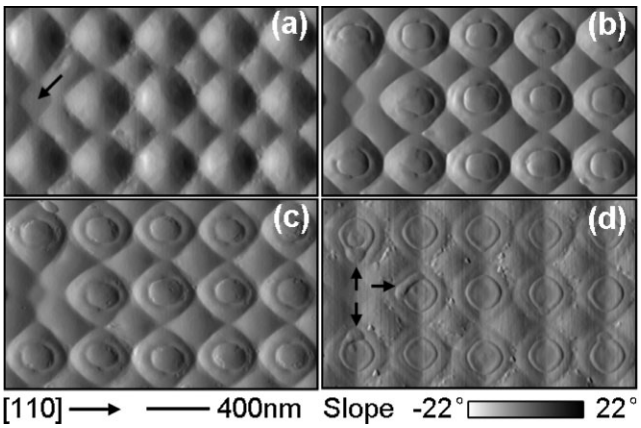

Figure 9 Sequence of AFM images of the same surface area of the annealed sample prior to etching (a) and after 60 min (b), 150 min (c), and 500 min (d) etching in NHH. The arrow in (a) marks an unoccupied site of the pattern. Arrows in (d) mark residual Si-rich material after almost complete SiGe etching. See Fig. 4 for more details on the sample. After Ref. [56].

3.3 Compositional profiles of SiGe islands after annealing In Section 2.3, we showed that, on patterned substrates, the coarsening is effectively suppressed and the size homogeneity is well preserved after annealing. The question now is: How does intermixing take place on the patterned substrates? Figure 9 shows AFM images of the annealed sample prior to etching (a) and after 60 min (b), 150 min (c), and 500 min (d) wet chemical etching in NHH. From the etching results, we can see that for most of the islands the SiGe has been etched away symmetrically, indicating that intermixing occurs in a symmetric fashion. In contrast, on planar substrates the intermixing takes place asymmetrically in conjunction with lateral island motion, which is self-sustaining once triggered by small composition fluctuations or environmental asymmetries [9, 28, 29]. The image in Fig. 9(d), taken after almost complete removal of the SiGe material, shows no trace of the "half-moon" shaped Si structures that occur when there is lateral island motion [28, 29]. We conclude that pits effectively "pin" the island position, because the center of the pit is an energetically favorable site [66–69]. A similar behavior was previously observed for annealing of closely-spaced vertically stacked islands, where the local energy minimum is provided by the tensile strain above buried islands [29].

On the other hand, islands in an asymmetric environment due to fabrication imperfections [see, *e.g.*, empty site marked in Fig. 9(a)] show a slightly asymmetric shape after annealing. The composition profiles are also asymmetric: the regions of the islands close to the empty site are etched less than the other regions, *i.e.*, they are richer in Si [see Fig. 9(b) and residual material pointed at by arrows in Fig. 9(d)]. It is natural that a strongly asymmetric environment would break the symmetry of the intermixing to some extent. However, even for these islands no evidence of lateral motion is seen.

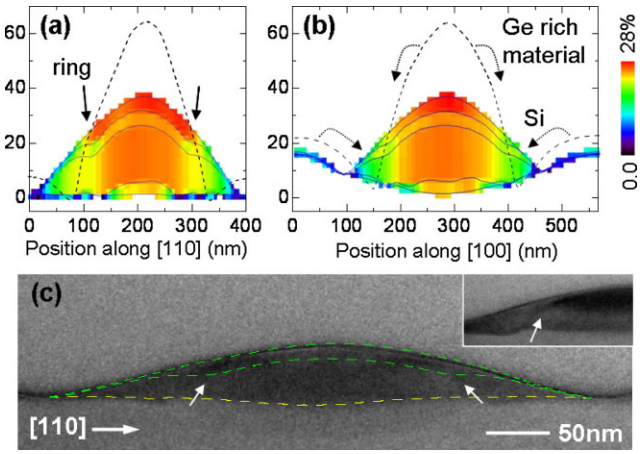

Figure 10 (online color at: www.pss-b.com) Cross-section through the center of an annealed island, showing Ge distributions obtained from the linescans shown as solid lines along (110) (a) and (100) (b) directions. Linescans of an as-grown island are included as dashed lines for comparison. (c) Bright field cross-sectional TEM images of an annealed island. Some of the AFM linescans from (a) are superimposed in (c) (dashed green lines), along with a linescan (dashed yellow line) obtained after complete SiGe removal in BPA solution. The inset shows the interface region at higher magnification. Arrows in (a), (c) mark the positions of the "rings" seen in Fig. 9(b), while arrows in (b) illustrate the material transfer occurring during annealing.

An interesting feature observed in Fig. 9(b, c) is a ring-shaped depression on the surface of partially etched islands. What is the origin of these "rings"? After annealing, the island base widens to cover nearly the whole pit and the island height decreases. Simultaneously, surrounding Si is incorporated into the island and the Si surface level drops correspondingly. Figure 10(a) and (b) show cross-sections of the Ge distributions on $(1\bar{1}0)$ and (010) planes passing through the center of an annealed island, respectively. The AFM linescans taken at different etching times (0, 60, 150, 420, and 500 min) in NHH solution which were used to evaluate the composition are also shown. The kinks in the linescans [see arrows in Fig. 10(a)] reflect local variations in the etching rate – faster at the island center and slower at the island boundary, which means a Ge rich core and Si rich shell around the base. We ascribe the Ge rich core to the original as-grown island and the Si rich shell to the alloyed SiGe region which develops during annealing. This interpretation is supported by the comparison between the linescans of islands after annealing and etching and linescans of an as-grown island, which are shown by dashed lines in Fig. 10(a) and (b). Although the relative vertical offset of the two sets of linescans is somewhat arbitrary, it is reasonable to assume that "rings" correspond to the interface between the original surface of the as-grown island and the strongly alloyed shell. We have confirmed this scenario using cross-sectional TEM. Figure 10(c) shows a bright field TEM image, and its inset shows a higher magnification image featuring the interface. Only the electrons from the (000) spot were used and the sample was tilted slightly away from the zone axis to minimize the diffraction contrast and thus the strain contrast. The main contrast of the image is the mass-thickness contrast, *i.e.*, dark areas contain heavier atoms or are thicker. The AFM linescans obtained prior to etching and after 150 min etching in NHH solution are superimposed on the TEM image (dashed green lines). Additionally an AFM linescan obtained after complete removal of the SiGe layer by 2 min etching in BPA solution [28, 70] is displayed as a dashed yellow line. The latter represents the interface between the island and the Si substrate, as indicated by the good agreement with the abrupt contrast change seen in the TEM image. Furthermore, in correspondence with the position of the "ring" [see arrows in Fig. 10(c) and inset], we can see a subtle change in contrast in the TEM image, which we can interpret as the boundary between the original Ge-rich island and the Ge-poor shell forming during annealing.

We can now provide a comprehensive picture of the evolution of islands upon annealing, with reference to Fig. 10(b). Before annealing, islands are generally characterized by a Ge distribution such that the Ge content decreases from the island top toward the base [32, 62]. Annealing causes additional Si–Ge intermixing driven by entropy increase, and also by strain energy reduction [9, 28, 71]. Although some bulk-like diffusion may occur during annealing [65], a dilute alloy can be efficiently obtained by surface diffusion if Si from the surrounding area mixes with Ge taken from the island surface and the mixture is deposited somewhere else, leaving uncovered Ge available for further mixing. From an energetic point of view, taking Ge away from the island top and depositing on the sides together with Si from the surrounding areas seems the most natural path. This lowers the surface area and surface energy, providing the flatter aspect ratio favored by more dilute SiGe [27], while leaving the most Ge-rich region exposed for further mixing. This pathway is fully consistent with our observations [see arrows in Fig. 10(b)]. The island height decreases as material is removed, and the island base broadens as the diluted mixture accumulates in a Si-rich shell bounded by extended {105} facets. This shell explains the ring-like depression in our etching experiments: the remainder of the original island is richer in Ge, so it etches faster than the surrounding shell. On planar substrates, material is removed from one side of the island and the diluted mixture is deposited on the other side. However, such lateral motion in unfavorable on the patterned substrate, where the pit effectively "pins" the island position.

4 Devices A DotFETs with enhanced electron mobility based on site-controlled SiGe islands has been demonstrated [72, 73]. The growth was performed as follows: after a 36 nm Si buffer growth (boron-doped, $\sim 1 \times 10^{17}\,\mathrm{cm}^{-3}$) on electron-beam patterned p-type Si(001) wafer with a pit period of 800 nm, 6 ML Ge were deposited at 720 °C and uniform dome-shaped SiGe islands with a diameter of 250 nm were obtained. Afterwards, a 30 nm Si cap (boron-

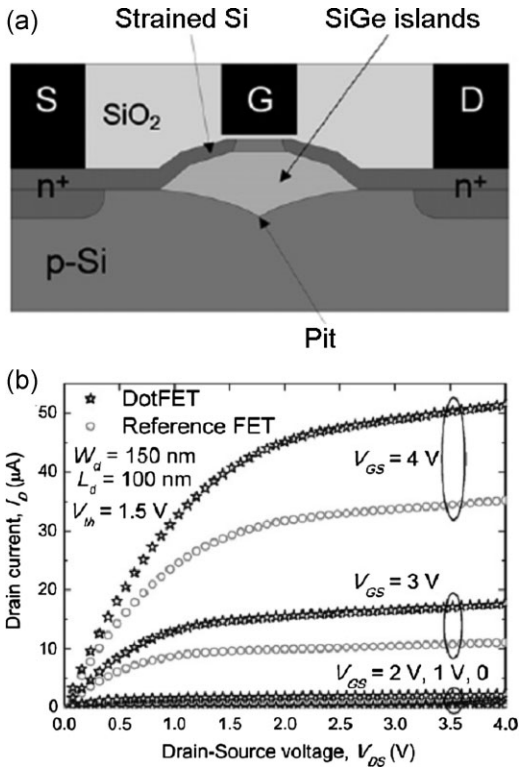

Figure 11 (a) Schematic cross-section of DotFET structure; (b) output characteristics of a DotFET and a reference FET with designed width W_d and length L_d of the short-gate segment of 150 and 100 nm, respectively. After Refs. [72, 73].

doped, $\sim 1 \times 10^{18}\,\mathrm{cm}^{-3}$) was deposited at a lower temperature of 360 °C to avoid intermixing with the buried SiGe islands. The n-channel DotFETs are fabricated in the center of the dot structure with all subsequent process steps being kept below 400 °C. Figure 11(a) shows the schematic cross-section of the DotFET. A detailed description of the process flow can be found in Refs. [72, 73]. To allow an estimation of the mobility enhancement, a set of reference devices were fabricated on the same wafer as the DotFETs using an identical layout, but without the underlying SiGe islands. Figure 11(b) shows the output characteristics of a DotFET and a reference field effect transistor (FET) at three different source–gate voltages. We see an increase in the drain current in the DotFET of 46% at $V_{GS} = V_{DS} = 4$ V.

By applying a focused synchrotron X-ray beam on this functioning DotFET, the composition profiles and the strain fields in and around a single SiGe island have been determined very recently, showing an average Ge content of ~40% and a maximum tensile strain of ~1% in the source-drain direction within the active region of the Si cap [42]. We note that the Ge content here (~40%) is higher than that shown in Fig. 7(b) (~30%) and attribute the difference to the higher Ge deposition rate (0.05 Å/s) and larger pit period used here. In fact a larger pit period implies a larger capture zone and therefore a larger Ge incorporation rate at a given deposition rate [51]. Due to the geometry of the gate stack (the Al-gatefinger and its interaction with the SiO_2 layer), it applies compressive strain to the Si cap directly underneath the gate and leads to a local decrease of the strain in the Si cap layer down to 0.3%, indicating it is essential to optimize the shape and material combinations of the gate stack [42].

5 Closely stacked islands to enhance tensile strain In order to further increase the tensile strain in the Si cap and correspondingly the transistor characteristics, one should optimize on one hand the structure of the gate stack as discussed above, and on the other hand we need to further increase the Ge fraction or the size of the SiGe islands [12, 50]. Although the Ge fraction in the SiGe islands increases approximately linearly with decreasing temperature, the island width decreases quadratically [74]. Therefore, strain maximization requires a careful choice of growth parameters yielding large and relatively Ge-rich islands. We address this issue by fabricating site-controlled arrays of two closely-stacked SiGe/Si island layers. The first layer is grown at a relatively high substrate temperature on pit-patterned Si(001) substrates to guarantee accurate position control, while the Si spacer and second Ge layer are grown at lower temperatures to obtain Ge-rich islands [75].

2D pit arrays with a period of 400 nm were patterned by holographic lithography and the samples were grown by MBE. After Si buffer growth, 15 ML Ge were deposited at a substrate temperature of 720 °C. For the double-layer sample, the first island layer was followed by the growth, at 620 °C, of 12 nm Si spacer layer and 9 ML Ge. The growth rates for Si and Ge were 1.0 and 0.05 Å/s, respectively [75].

Figure 12(a) shows a bright field cross-sectional TEM image of two stacked islands. The main contrast of the image is the mass-thickness contrast, *i.e.*, dark areas contain heavier atoms or are thicker. We see that the two islands are connected, and, most importantly, that they have similar sizes but markedly different Ge content, with the top island being Ge-richer. To quantify the Ge fraction profile in the topmost islands, we employed again nanotomography [44]. Figure 12(b) shows AFM linescans obtained at different stages of NHH etching and the derived cross-sectional Ge distribution on the (110) plane passing through the island center. The graph shows that the Ge content increases from 0.42 to 0.52 along the growth direction. The average Ge content of the top island layer is about 0.46, which is ~50% higher than the Ge fraction of islands in the first Ge layer.

As a consequence of the increased Ge fraction, we expect that they induce a larger tensile strain in a Si cap layer compared to a single SiGe island layer. Figure 12(e) shows the in-plane strain distribution on the cross-sectional (110) plane passing through the center of stacked islands with 20 nm Si cap layer. We assumed that the 20 nm Si layer covers the islands conformally, which can be experimentally realized by low temperature (~300 °C) capping [76, 77]. The strain was calculated by finite element method (FEM) with the realistic input structure. The Ge composition profiles were taken from experiment for the top island [Fig. 12(b)]

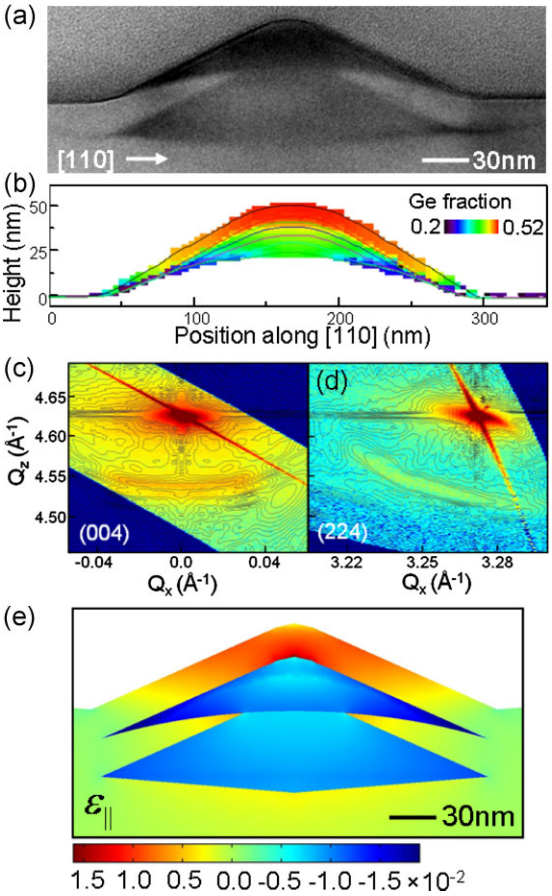

Figure 12 (online color at: www.pss-b.com) (a) Bright field cross-sectional TEM image of two closely stacked islands. (b) Cross-sectional Ge distribution along (110) direction passing through the island center obtained by selective etching in NHH solution. (c) and (d) Experimental XRD patterns (color plots) and calculated intensities (contours) around the (004) and (224) Bragg points, respectively. (e) Calculated in-plane strain distribution for closely stacked islands with 20 nm Si cap on the cross-sectional (110) plane passing through island center. After Ref. [75].

and from a reference sample prior to overgrowth (Ge content increasing from 0.22 to 0.35 along the growth direction) for the bottom island. Experimentally recorded XRD patterns around the (004) and (224) Bragg points [color plots in Fig. 12(c) and (d)] are compared to diffraction intensities calculated based on input from FEM simulations [contours in Fig. 12(c) and (d)]. These calculations are in very good agreement with the measured XRD data, supporting the accuracy of nanotomography. From Fig. 12(e), we see that the Si cap is tensile strained with a maximum value of 1.57%, which is a factor of 2 higher than that induced by islands only after the first Ge layer growth.

6 Conclusions We have investigated the morphological and compositional evolution of site-controlled SiGe islands on 2D pit-patterned Si(001) substrates. On pit-patterned substrates, the driving force for coarsening is effectively reduced and the presence of pits allows the fabrication of uniform island arrays with any of their equilibrium shapes (prepyramids, pyramids, transition domes, domes, barns). Islands on patterned substrates show symmetric shapes and composition distributions even for patterns with rectangular lattice. In addition, island arrays show not only morphologically but also compositionally homogeneity, at least for the 2D square and rectangular lattices studied here. With increasing Ge deposition or even after post-growth annealing, all islands on patterned substrates evolve simultaneously in size, shape, and composition. During annealing, the substrate patterning pins the island position and suppresses the lateral motion, which was generally observed on flat substrates. Based on site-controlled SiGe islands, an n-channel MOSFET with enhanced electron mobility has been demonstrated. To further increase the tensile strain and correspondingly the electron mobility, a new approach with closely stacked SiGe islands grown at different temperatures has been presented.

Acknowledgements We acknowledge the financial support by the EC d-DOTFET project (No. 012150) and by the DFG (FOR730 and SPP1386, project RA 1634/5-1) and fruitful collaboration with G. Chen, N. Hrauda, H. Groiss, J. Stangl, L. K. Nanver, V. Jovanović, D. Grützmacher, M. Stoffel, G. Katsaros, J. Tersoff, L. Miglio, F. Schäffler on different aspects of this work.

References

[1] J. Stangl, V. Holý, and G. Bauer, Rev. Mod. Phys. **76**, 725 (2004).
[2] Y.-W. Mo, D. E. Savage, B. S. Swartzentruber, and M. G. Lagally, Phys. Rev. Lett. **65**, 1020 (1990).
[3] T. I. Kamins, E. C. Carr, R. S. Willams, and S. J. Rosner, J. Appl. Phys. **81**, 211 (1997).
[4] G. Medeiros-Ribeiro, A. M. Bratkovski, T. I. Kamins, D. A. A. Ohlberg, and R. S. Williams, Science **279**, 353 (1998).
[5] F. M. Ross, R. M. Tromp, and M. C. Reuter, Science **286**, 1931 (1999).
[6] F. Montalenti, P. Raiteri, D. B. Migas, H. von Känel, A. Rastelli, C. Manzano, G. Costantini, U. Denker, O. G. Schmidt, K. Kern, and L. Miglio, Phys. Rev. Lett. **93**, 216102 (2004).
[7] F. M. Ross, J. Tersoff, and R. M. Tromp, Phys. Rev. Lett. **80**, 984 (1998).
[8] A. Rastelli, M. Stoffel, U. Denker, T. Merdzhanova, and O. G. Schmidt, Phys. Status Solidi A **203**, 3506 (2006).
[9] Y. Tu and J. Tersoff, Phys. Rev. Lett. **98**, 096103 (2007).
[10] M. S. Leite, A. Malachias, S. W. Kycia, T. I. Kamins, R. S. Williams, and G. Medeiros-Ribeiro, Phys. Rev. Lett. **100**, 226101 (2008).
[11] O. G. Schmidt and K. Eberl, IEEE Trans. Electron Devices **48**, 1175 (2001).
[12] R. A. Donaton, D. Chidambarrao, J. Johnson, P. Chang, Y. Liu, W. K. Henson, J. Holt, X. Li, J. Li, A. Domenicucci, A. Madan, K. Rim, and C. Wann, Tech. Dig. – Int. Electron Devices Meet., 2006, p. 465.
[13] K. W. Ang, C. H. Tung, N. Balasubramanian, G. S. Samudra, and Y. C. Yeo, IEEE Electron Device Lett. **28**, 609 (2007).

[14] G. Katsaros, P. Spathis, M. Stoffel, F. Fournel, M. Mongillo, V. Bouchiat, F. Lefloch, A. Rastelli, O. G. Schmidt, and S. De Franceschi, Nature Nanotechnol. **5**, 458 (2010).
[15] G. Pernot, M. Stoffel, I. Savic, F. Pezzoli, P. Chen, G. Savelli, A. Jacquot, J. Schumann, U. Denker, I. Mönch, Ch. Deneke, O. G. Schmidt, J. M. Rampnoux, S. Wang, M. Plissonnier, A. Rastelli, S. Dilhaire, and N. Mingo, Nature Mater. **9**, 491 (2010).
[16] V. Lavchiev, R. Holly, G. Chen, F. Schäffler, R. Goldhahn, and W. Jantsch, Opt. Lett. **34**, 3785 (2009).
[17] D. Grützmacher, T. Fromherz, C. Dais, J. Stangl, E. Müller, Y. Ekinci, H. H. Solak, H. Sigg, R. Lechner, E. Wintersberger, S. Birner, V. Holy, and G. Bauer, Nano Lett. **7**, 3150 (2007).
[18] O. G. Schmidt (ed.), Lateral Alignment of Epitaxial Quantum Dots (Springer, Berlin, 2007).
[19] G. Jin, J. L. Liu, S. G. Thomas, Y. H. Luo, and K. L. Wang, Appl. Phys. Lett. **75**, 2752 (1999).
[20] Z. Zhong, A. Halilovic, M. Mühlberger, F. Schäffler, and G. Bauer, J. Appl. Phys. **93**, 6258 (2003).
[21] G. S. Kar, S. Kiravittaya, M. Stoffel, and O. G. Schmidt, Phys. Rev. Lett. **93**, 246103 (2004).
[22] E. S. Kim, N. Usami, and Y. Shiraki, Appl. Phys. Lett. **72**, 1617 (1998).
[23] O. G. Schmidt, N. Y. Jin-Phillipp, C. Lange, U. Denker, K. Eberl, R. Schreiner, H. Gräbeldinger, and H. Schweizer, Appl. Phys. Lett. **77**, 4139 (2000).
[24] Z. Zhong, A. Halilovic, M. Mühlberger, F. Schäffler, and G. Bauer, Appl. Phys. Lett. **82**, 4779 (2003).
[25] C. Dais, H. H. Solak, Y. Ekinci, E. Müller, H. Sigg, and D. Grützmacher, Surf. Sci. **601**, 2787 (2007).
[26] Z. Zhong and G. Bauer, Appl. Phys. Lett. **84**, 1922 (2004).
[27] T. I. Kamins, G. Medeiros-Ribeiro, D. A. A. Ohlberg, and R. Stanley Williams, J. Appl. Phys. **85**, 1159 (1999).
[28] U. Denker, A. Rastelli, M. Stoffel, J. Tersoff, G. Katsaros, G. Costantini, K. Kern, N. Y. Jin-Phillipp, D. E. Jesson, and O. G. Schmidt, Phys. Rev. Lett. **94**, 216103 (2005).
[29] M. Stoffel, A. Rastelli, S. Kiravittaya, and O. G. Schmidt, Phys. Rev. B **72**, 205411 (2005).
[30] T. U. Schülli, M. Stoffel, A. Hesse, J. Stangl, R. T. Lechner, E. Wintersberger, M. Sztucki, T. H. Metzger, O. G. Schmidt, and G. Bauer, Phys. Rev. B **71**, 035326 (2005).
[31] R. Magalhães-Paniago, G. Medeiros-Ribeiro, A. Malachias, S. Kycia, T. I. Kamins, and R. Stanley Williams, Phys. Rev. B **66**, 245312 (2002).
[32] A. Malachias, S. Kycia, G. Medeiros-Ribeiro, R. Magalhães-Paniago, T. I. Kamins, and R. Stanley Williams, Phys. Rev. Lett. **91**, 176101 (2003).
[33] F. Ratto, F. Rosei, A. Locatelli, S. Cherigi, S. Fontana, S. Heyn, P.-D. Szkutnik, A. Sgarlata, M. De Crescenzi, and N. Motta, J. Appl. Phys. **97**, 043516 (2005).
[34] G. Biasiol, S. Heun, G. B. Golinelli, A. Locatelli, T. O. Mentes, F. Z. Guo, C. Hofer, C. Teichert, and L. Sorba, Appl. Phys. Lett. **87**, 223106 (2005).
[35] M. Floyd, Y. Zhang, K. P. Driver, J. Drucker, P. A. Crozier, and D. J. Smith, Appl. Phys. Lett. **82**, 1473 (2003).
[36] M. Schade, F. Heyroth, F. Syrowatka, H. S. Leipner, T. Boeck, and M. Hanke, Appl. Phys. Lett. **90**, 263101 (2007).
[37] P. Offermans, P. M. Koenraad, J. H. Wolter, K. Pierz, M. Roy, and P. A. Maksym, Phys. Rev. B **72**, 165332 (2005).
[38] G. Springholz, L. Abtin, and V. Holy, Appl. Phys. Lett. **90**, 113119 (2007).
[39] N. A. Katcho, M. I. Richard, M. G. Proietti, H. Renevier, C. Leclere, V. Favre-Nicolin, J. J. Zhang, and G. Bauer, Europhys. Lett. **93**, 66004 (2011).
[40] I. Arslan, T. J. V. Yates, N. D. Browning, and P. A. Midgley, Science **309**, 2195 (2005).
[41] T. Inoue, T. Kita, O. Wada, M. Konno, T. Yaguchi, and T. Kamino, Appl. Phys. Lett. **92**, 031902 (2008).
[42] N. Hrauda, J. J. Zhang, E. Wintersberger, T. Etzelstorfer, B. Mandl, J. Stangl, D. Carbone, V. Holy, V. Jovanovic, C. Biasotto, L. K. Nanver, J. Moers, D. Grützmacher, and G. Bauer, Nano Lett. **11**, 2875 (2011).
[43] M. Dubslaff, M. Hanke, S. Schöder, M. Burghammer, T. Boeck, and J. Patommel, Appl. Phys. Lett. **96**, 133107 (2010).
[44] A. Rastelli, M. Stoffel, A. Malachias, T. Merdzhanova, G. Katsaros, K. Kern, T. H. Metzger, and O. G. Schmidt, Nano Lett. **8**, 1404 (2008).
[45] J. J. Zhang, F. Montalenti, A. Rastelli, N. Hrauda, D. Scopece, H. Groiss, J. Stangl, F. Pezzoli, F. Schäffler, O. G. Schmidt, L. Miglio, and G. Bauer, Phys. Rev. Lett. **105**, 166102 (2010).
[46] F. Schäffler, Semicond. Sci. Technol. **12**, 1515 (1997).
[47] J. L. Hoyt, H. M. Nayfeh, S. Eguchi, I. Aberg, G. Xia, T. Drake, E. A. Fitzgerald, and D. A. Antoniadis, Tech. Dig. – Int. Electron Devices Meet., 2002, p. 23.
[48] M. L. Lee, E. A. Fitzgerald, M. T. Bulsara, M. T. Currie, and A. Lochtefeld, J. Appl. Phys. **97**, 011101 (2005).
[49] P. Packan, S. Akbar, M. Armstrong, D. Bergstrom, M. Brazier, H. Deshpande, K. Dev, G. Ding, T. Ghani, O. Golonzka, W. Han, J. He, R. Heussner, R. James, J. Jopling, C. Kenyon, S. H. Lee, M. Liu, S. Lodha, B. Mattis, A. Murthy, L. Neiberg, J. Neirynck, S. Pae, C. Parker, L. Pipes, J. Sebastian, J. Seiple, B. Sell, A. Sharma, S. Sivakumar, B. Song, A. St. Amour, K. Tone, T. Troeger, C. Weber, K. Zhang, Y. Luo, and S. Natarajan, Tech. Dig. – Int. Electron Devices Meet., 2009, p. 659.
[50] J. G. Fiorenza, J. S. Park, and A. Lochtefeld, IEEE Trans. Electron Devices **55**, 640 (2008).
[51] J. J. Zhang, M. Stoffel, A. Rastelli, O. G. Schmidt, V. Jovanović, L. K. Nanver, and G. Bauer, Appl. Phys. Lett. **91**, 173115 (2007).
[52] J. J. Zhang, Growth and characterization of ordered SiGe islands on patterned Si(001) substrates, Ph.D. thesis, Institut für Halbleiterphysik, Johannes Kepler Universität Linz, 2010.
[53] A. Rastelli, H. von Känel, B. J. Spencer, and J. Tersoff, Phys. Rev. B **68**, 115301 (2003).
[54] Z. Zhong, O. G. Schmidt, and G. Bauer, Appl. Phys. Lett. **87**, 133111 (2005).
[55] M. Stoffel, A. Rastelli, J. Tersoff, T. Merdzhanova, and O. G. Schmidt, Phys. Rev. B **74**, 155326 (2006).
[56] J. J. Zhang, A. Rastelli, H. Groiss, J. Tersoff, F. Schäffler, O. G. Schmidt, and G. Bauer, Appl. Phys. Lett. **95**, 183102 (2009).
[57] M. A. Lutz, R. M. Feenstra, P. M. Mooney, J. Tersoff, and I. O. Chu, Surf. Sci. **316**, L1075 (1994).
[58] C. Dais, G. Mussler, H. Sigg, E. Müller, H. H. Solak, and D. Grützmacher, J. Appl. Phys. **105**, 122405 (2009).
[59] J. J. Zhang, A. Rastelli, O. G. Schmidt, and G. Bauer, Appl. Phys. Lett. **97**, 203103 (2010).
[60] M. Stoffel, A. Malachias, T. Merdzhanova, F. Cavallo, G. Isella, D. Chrastina, H. von Känel, A. Rastelli, and O. G. Schmidt, Semicond. Sci. Technol. **23**, 085021 (2008).

[61] G. Katsaros, A. Rastelli, M. Stoffel, G. Isella, H. von Känel, A. M. Bittner, J. Tersoff, U. Denker, O. G. Schmidt, G. Costantini, and K. Kern, Surf. Sci. **600**, 2608 (2006).
[62] T. U. Schülli, G. Vastola, M.-I. Richard, A. Malachias, G. Renaud, F. Uhlík, F. Montalenti, G. Chen, L. Miglio, F. Schäffler, and G. Bauer, Phys. Rev. Lett. **102**, 025502 (2009).
[63] U. Denker, M. Stoffel, and O. G. Schmidt, Phys. Rev. Lett. **90**, 196102 (2003).
[64] G. Katsaros, G. Costantini, M. Stoffel, R. Esteban, A. M. Bittner, A. Rastelli, U. Denker, O. G. Schmidt, and K. Kern, Phys. Rev. B **72**, 195320 (2005).
[65] M. S. Leite, G. Medeiros-Ribeiro, T. I. Kamins, and R. S. Williams, Phys. Rev. Lett. **98**, 165901 (2007).
[66] G. Vastola, F. Montalenti, and L. Miglio, J. Phys.: Condens. Matter **20**, 454217 (2008).
[67] H. Hu, H. J. Gao, and F. Liu, Phys. Rev. Lett. **101**, 216102 (2008).
[68] Z. Zhong, W. Schwinger, F. Schäffler, G. Bauer, G. Vastola, F. Montalenti, and L. Miglio, Phys. Rev. Lett. **98**, 176102 (2007).
[69] G. Katsaros, J. Tersoff, M. Stoffel, A. Rastelli, P. Acosta-Diaz, G. S. Kar, G. Costantini, O. G. Schmidt, and K. Kern, Phys. Rev. Lett. **101**, 096103 (2008).
[70] T. K. Carns, M. O. Tanner, and K. L. Wang, J. Electrochem. Soc. **142**, 1260 (1995).
[71] G. Medeiros-Ribeiro and R. Stanley Williams, Nano Lett. **7**, 223 (2007).
[72] V. Jovanović, C. Biasotto, L. K. Nanver, J. Moers, D. Grützmacher, J. Gerharz, G. Mussler, J. van der Cingel, J. J. Zhang, G. Bauer, O. G. Schmidt, and L. Miglio, IEEE Electron Device Lett. **31**, 1083 (2010).
[73] L. K. Nanver, V. Jovanović, C. Biasottoa, J. Moers, D. Grützmacher, J. J. Zhang, N. Hrauda, M. Stoffel, F. Pezzoli, O. G. Schmidt, L. Miglio, H. Kosina, A. Marzegalli, G. Vastola, G. Mussler, J. Stangl, G. Bauer, J. van der Cingel, and E. Bonera, Solid State Electron. **60**, 75 (2011).
[74] G. Capellini, M. De Seta, and F. Evangelisti, Appl. Phys. Lett. **78**, 303 (2001).
[75] J. J. Zhang, N. Hrauda, H. Groiss, A. Rastelli, J. Stangl, F. Schäffler, O. G. Schmidt, and G. Bauer, Appl. Phys. Lett. **96**, 193101 (2010).
[76] A. Rastelli, E. Müller, and H. von Känel, Appl. Phys. Lett. **80**, 1438 (2002).
[77] N. Hrauda, J. J. Zhang, J. Stangl, A. Rehman-Khan, G. Bauer, M. Stoffel, O. G. Schmidt, V. Jovanovich, and L. K. Nanver, J. Vac. Sci. Technol. B **27**, 912 (2009).